Probing core and shell contributions to exchange bias in Co/Co_3O_4 nanoparticles of controlled size

D. De,[1,2] Òscar Iglesias,[3,*] S. Majumdar,[1] and Saurav Giri[1,†]

[1]*Department of Solid State Physics, Indian Association for the Cultivation of Science, Jadavpur, Kolkata 700032, India*

[2]*Department of Physics, The Neotia University, D. H. Road, 24 PGS (S), W.B. 743368, India*

[3]*Departament de Física de la Matèria Condensada and Institut de Nanociència i Nanotecnologia (IN^2UB), Facultat de Física, Universitat de Barcelona, Av. Diagonal 647, 08028 Barcelona, Spain*

(Received 1 July 2016; revised manuscript received 19 October 2016; published 11 November 2016)

Coupling at the interface of core/shell magnetic nanoparticles is known to be responsible for exchange bias (EB) and the relative sizes of core and shell components are supposed to influence the associated phenomenology. In this work, we have prepared core/shell structured nanoparticles with a total average diameter around ∼27 nm and a wide range of shell thicknesses through the controlled oxidation of Co nanoparticles well dispersed in an amorphous silica host. Structural characterizations give compelling evidence of the formation of Co_3O_4 crystallite phase at the shells surrounding the Co core. Field cooled hysteresis loops display nonmonotonous dependence of the exchange bias H_E and coercive H_C fields, that become maximum for a sample with an intermediate shell thickness, at which lattice strain is also maximum for both phases. The EB effects persist up to temperatures above the ordering temperature of the oxide shell. Results of our atomistic Monte Carlo simulations of particles with the same size and composition as in experiments are in agreement with the experimental observations and have allowed us to identify a change in the contribution of the interfacial surface spins to the magnetization reversal, giving rise to the observed maximum in H_E and H_C.

DOI: 10.1103/PhysRevB.94.184410

I. INTRODUCTION

Nanocrystalline materials are of potential interest nowadays, because their remarkable properties, that differ from their parent bulk counterparts, have found a wide range of technological applications. Among them, particles made of magnetic compounds display a variety of magnetic behaviors, that differ substantially from their parent massive materials [1–3]. Their distinct properties are mainly connected to the finite size effects related to the reduced number of magnetic ions in the enclosed volume [4]. Additionally, surface and interface effects related to the symmetry breaking at physical boundaries of the materials cause spin disorder and frustration along with the interparticle interactions [5]. An interesting class of nanoparticles (NP) is found when ferromagnetic (FM) and antiferromagnetic (AF) materials are combined together in a core/shell structure. The coupling at the interface between these two magnetic phases gives rise to the EB phenomenon [6–10], which is of fundamental interest and has found multiple technological applications depending on the specific composition and the characteristic size of the respective phases [11–16]. The pinning mechanism, that results from EB, has been commercially explored for magnetic field sensors and in modern magnetic read heads [17,18]. Nevertheless, a clearcut connection between the observed EB phenomenology and parameters in core/shell NP, such as size and thickness of the NP, or the microscopic interfacial structure, is not well established yet.

Although pure metal particles would have desirable high values of saturation of magnetization [19], they have strong natural tendency to form parent oxide phases [20,21]. This process can be controlled under proper synthesis conditions to prevent further oxidation, leading to the formation of core/shell structures with the oxide phase (often an AF or ferrimagnetic material [22]) usually formed at the outer part of the structures. In the case of Co NP, most of the published studies [23] report the formation of the CoO phase on the shell, although in some cases the presence of the Co_3O_4 has also been evidenced by structural [24,25] or magnetic characterization [26], The possibility of observing EB in Co based nanostructures in contact with Co_3O_4 has been rather less investigated and the published studies focus on layered structures [27–31]. Synthesis of single phase CoO or Co_3O_4 NP have been achieved by several authors, that have reported AF magnetic behavior with ordering temperatures reduced compared to the bulk values [32–34] and remanence values much higher than those for the bulk due to finite-size effects [26,35].

Here, we will explore the EB effect in Co/Co_3O_4 batches of nanoparticles with similar average size, giving evidences that Co_3O_4 is the only phase present in our samples. The sizes of the crystallites forming core and shell are tuned by the controlled oxidation at different temperatures. Hence we are able to show that the variation of shell thickness leads to significant changes in the EB effect that are stronger for intermediate shell thicknesses. A detailed structural study of the samples allows to correlate this maximum EB to the maximum interfacial strain due to lattice mismatch and the associated increased anisotropy. By means of atomistic Monte Carlo (MC) simulations, we trace back the origin of maximum EB effect at the intermediate size and the changes in the magnetization reversal of interfacial surface spins as core/shell size is varied.

II. EXPERIMENT

Nanocrystalline Co embedded in an amorphous silica host is prepared with volume fraction $\varphi = 10\%$ using sol gel route. Initially, Co metal powder (Aldrich, 99.99% pure) is

*oscar@ffn.ub.es; http://www.ffn.ub.es/oscar

†sspsg2@iacs.res.in

dissolved in nitric acid (4.5 M). Citric acid is then added to the solution and homogenized thoroughly during 6 h to obtain a transparent reddish solution. Ethanolic tetraethyl orthosilicate (TEOS) is finally added to the solution as a source for the silica matrix in the form of droplets and mixed vigorously for 12 h for obtaining a homogeneous solution. The final reddish solution is dried in open air very slowly to form a gel at room temperature, that is dried at 323 K for 15 days and subsequently decomposed at 873 K for 6 h in a continuous flow of H_2/argon mixture (5% H_2 and 95% argon). The as-synthesized Co nanoparticles ($\varphi \sim 10\%$) in a silica matrix are processed for controlled oxidation by annealing the sample in the range of 333–1023 K for 10 min each in order to grow desired Co/Co_3O_4 phase fractions. Henceforth, nine samples will be addressed as 25:2, 24:3, 21:6, 18:9, 15:12, 10:17, 5:22, 2:25, and 1:26, where numbers are the sizes of Co and Co_3O_4 phases, respectively, in nm.

Chemical composition is confirmed using powder x-ray diffraction (XRD) studies (Seifert XRD 3000P) considering Cu $K\alpha$ radiation and electron diffraction attached with a transmission electron microscopy (TEM) of JEOL TEM 2010. High resolution TEM images of the particles are used to assess their size, shape, and crystalline planes of Co and Co_3O_4. X-ray photoemission spectroscopy (XPS) have been performed in an Omicron Nanotechnology spectrometer. Magnetization is recorded in a commercial SQUID magnetometer of Quantum Design (MPMS, XL). In the zero-field cooled (ZFC) protocol the sample is cooled in zero field and the magnetization is measured in the warming mode with a static magnetic field. In the field-cooled (FC) protocol sample is cooled and measured in field.

III. STRUCTURAL CHARACTERIZATION

XRD patterns of Co and Co/Co_3O_4 of selected samples with different phase fractions are depicted in Figs. 1(a)–1(d). The continuous curves show the corresponding fits obtained by Rietveld refinement with the MAUD software, using face-centered $Fm3m$ and $Fd3m$ space groups for Co and Co_3O_4, respectively. The details of the refinement are shown in Fig. 1(b), where the vertical bars at the bottom depict the diffraction peak positions of Co and Co_3O_4. The goodness of the fit is demonstrated by the difference plot shown below the diffraction patterns for all the compositions, which confirms absence of other impurity phases such as minor fraction of CoO. With increasing annealing temperature the Co_3O_4 phase grows at the expense of Co.

Average crystallite sizes of each component for different annealing temperatures are estimated using the Scherrer formula from broadening of the diffraction peaks, as obtained from the Rietveld refinement [36]. Individual average crystallite sizes of each component for annealing temperatures in the range 333–1023 K are depicted in Fig. 1(e). The obtained average particle size is around 27 nm for the different annealing temperatures. The lattice constants (a) as obtained from the Rietveld refinements are plotted as a function of the individual crystallite sizes in Fig. 1(f). The obtained values are consistent with the previously reported results [34,37]. For most of the samples the lattice constants of Co and Co_3O_4 deviate from their bulk counterpart values 3.54 and 8.09 Å [see dashed lines in 1(f)] [34,38], being higher and lower than in bulk, respectively. This reveals significant tensile strains on the Co cores of the particles caused by the formation of the oxide phase at the shell. Interestingly, a maximum value of both a is found for the sample obtained at an annealing temperature of 473 K, with crystallite sizes ~18 and ~9 nm for Co and Co_3O_4, respectively.

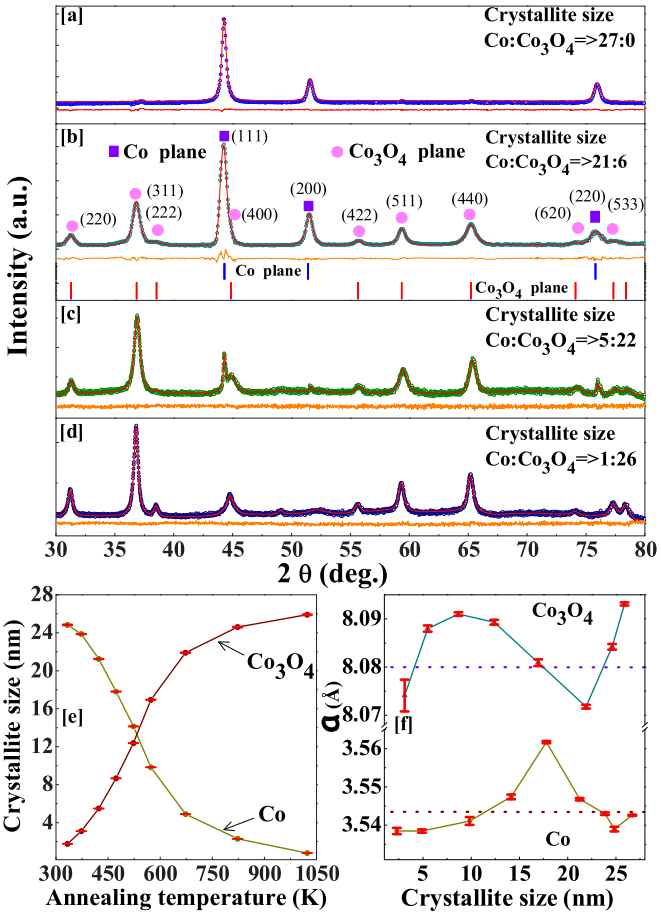

FIG. 1. (a)–(d) XRD patterns of Co/Co_3O_4 nanostructures with different core/shell crystallite sizes. Continuous curves show the fit using Rietveld refinement. Difference plots are shown at the bottom of each pattern. Details of the indexed planes corresponding to Co and Co_3O_4 are given in (b) for the 21 : 6 sample. Variation of the (e) crystallite sizes of the two phases with the annealing temperatures and (f) lattice constant (a) of the two phases with the crystallite size, as obtained from the refinement (dashed lines indicate the bulk values).

Analysis of the XPS spectra have been performed in order to investigate the details of the chemical composition of the core and shell phases of the nanoparticles. The results for the Co $2p_{3/2}$ and O $1s$ contributions to XPS are depicted in Fig. 2(a) for the sample with 15 : 12 composition. The oxidation states of Co atoms are obtained by deconvoluting the spectra for Co $2p_{3/2}$ and O $1s$ contributions, as shown at the top and bottom panels of the figure. The Co^{2+}, Co^{3+}, and Co contributions to the $2p_{3/2}$ spectrum can be deconvoluted as shown in the corresponding subspectra (lines) that exhibit maxima with increasing binding energies, respectively. A similar procedure is done for the O $1s$ spectrum, that can be deconvoluted into four contributions, exhibiting maxima with

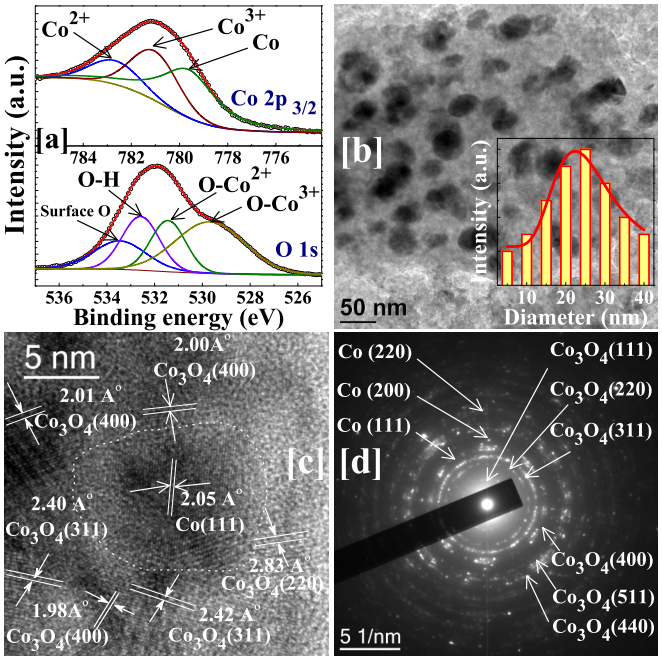

FIG. 2. (a) XPS spectrograms of Co $2p_{3/2}$ (top panel) and O 1s (bottom panel) contributions. (b) TEM image to verify particle size. Inset: particle size histogram as fitted by a log-normal distribution function. (c) High resolution TEM image displaying nearly core shell structure composed of Co and Co_3O_4, respectively. Different planes corresponding to Co and Co_3O_4 are depicted. (d) Electron diffraction pattern displaying different planes for 15 : 12 sample.

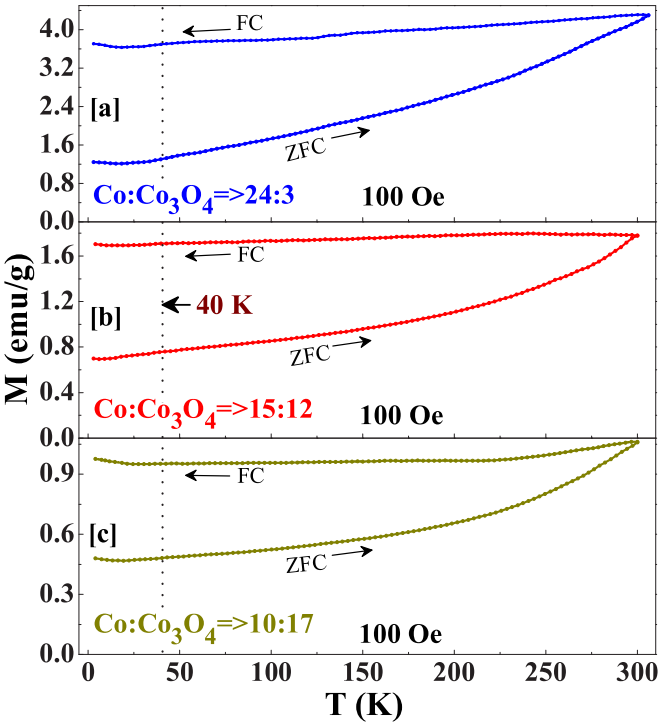

FIG. 3. Thermal variations of ZFC and FC magnetization for Co:Co_3O_4 with (a) 24 : 3, (b) 15 : 12, and (c) 10 : 17. The dotted line indicates the ordering temperature of bulk Co_3O_4.

increasing energy corresponding to surface O, O-H, O-Co^{2+}, and O-Co^{3+}, respectively. It is noted that the ratio of the area under the deconvoluted curves of Co^{3+} and Co^{2+} in Co $2p_{3/2}$ spectrum, as well as that of O-Co^{3+} and O-Co^{2+} curves in O 1s spectrum, has nearly the same value of 2 : 1, as expected for Co_3O_4. Furthermore, the analysis provides a ratio of Co : $(Co^{2+} + Co^{3+}) \approx 50.3 : 49.7$, which is close to the phase fraction ratio of Co : $Co_3O_4 \approx 52 : 48$, as obtained from the Rietveld refinement. These two observations clearly corroborate the absence of any detectable contribution from CoO as also indicated by the XRD analysis mentioned above.

Figure 2(b) shows a TEM image of the sample 15 : 12. As depicted in the inset, there is a distribution of particle sizes that can be fitted using log-normal distribution function with an average size of ∼24 nm (consistent with that observed from the XRD results) and tails that extend from 5 to 40 nm (continuous curve). A high resolution TEM image of a particle of the same sample is shown in Fig. 2(c), where we have indicated the distinct Co and Co_3O_4 areas within the particle. Moreover, we have identified the Co (111) diffraction planes within the darker core region and, outside, the distinctive planes of Co_3O_4, that could also be observed in the XRD patterns. These representative Co and Co_3O_4 planes can also be clearly resolved in the electron diffraction pattern shown in Fig. 2(d). All in all, careful structural analysis does not show any convincing signature CoO phase, consistent with the XRD results.

IV. MAGNETIC CHARACTERIZATION

The thermal variation of dc magnetization measured under ZFC and FC protocols with an applied magnetic field of 100 Oe are depicted in Figs. 3(a)–3(c) for samples 24 : 3, 15 : 12, and 10 : 17. The behavior of the three samples is similar, showing irreversibility up to the highest measured temperature of 300 K, which indicates that the nanoparticles have blocking temperatures above this value due to their relatively large size. Note that both curves decrease monotonously below 300 K and do not display any peak characteristic of the Néel temperature of CoO, which should be in the range of 235–293 K depending on the particle size [26,39,40]. However, below ∼40 K, a weak anomaly marked by an upturn of the magnetization can be observed in both the ZFC and FC curves, which could be ascribed to the onset of the antiferromagnetic order [26] in crystallites forming the shell since Co_3O_4 orders antiferromagnetically around 40 K [41]. This is consistent with the significant reduction of the Néel temperature of Co_3O_4 down to the range of 26–35 K (depending on the particle size) due to finite-size effects [34,42].

With increasing Co_3O_4 fraction, the magnitude of the magnetization decreases as a result of the increasing contribution of shell spins with reduced magnetization, as shown in Fig. 3. Similar low temperature responses (not to be confused with the ones reported here) have been reported that are usually ascribed either to residual phases [26] in Co/CoO nanoparticles or onset of spin-glass freezing [39,43] for other core/shell compositions.

Hysteresis loops have been measured in between ±20 kOe at 5 K for all the nine samples, as shown by the full

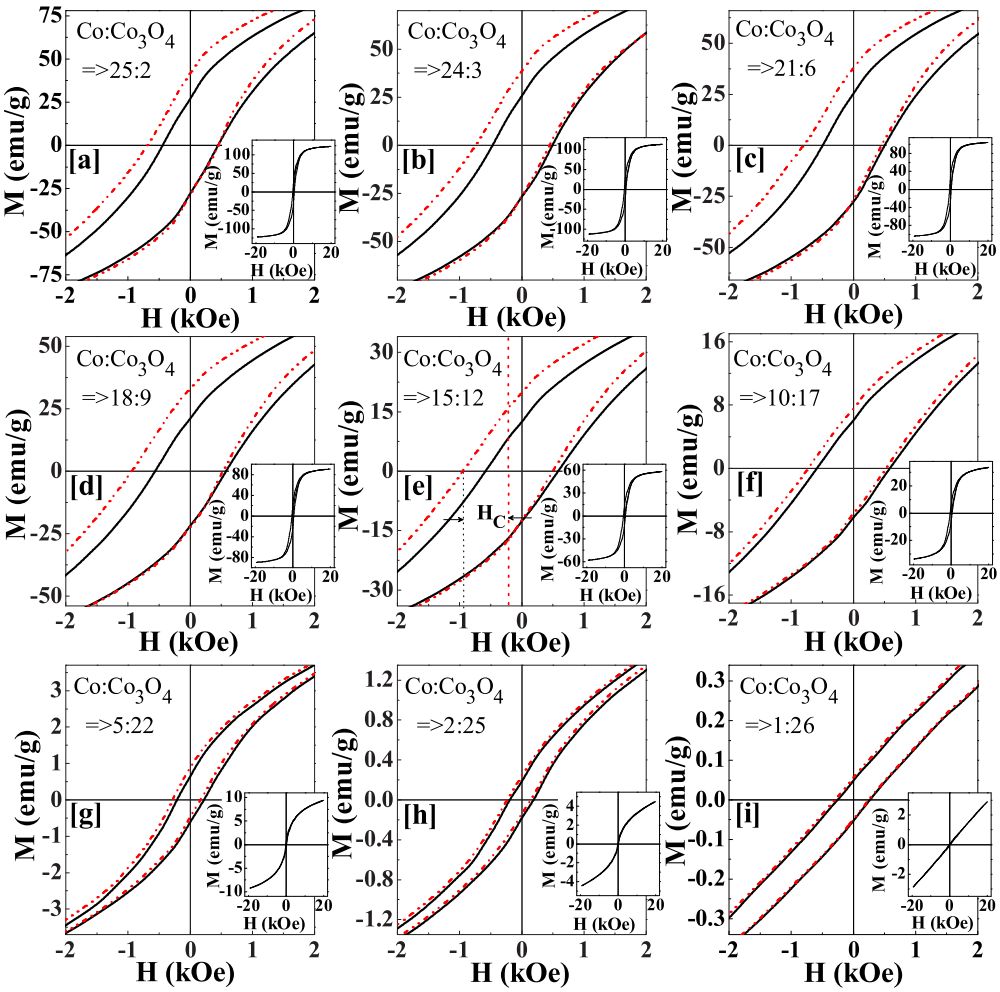

FIG. 4. Central portion of the field-cooled (dashed curve) and zero field-cooled (continuous curve) magnetic hysteresis loops at 5 K for Co:Co_3O_4 with crystallite sizes (in nm) (a) 25 : 2, (b) 24 : 3, (c) 21 : 6, (d) 18 : 9, (e) 15 : 12, (f) 10 : 17, (g) 5 : 22, (h) 2 : 25, and (i) 1 : 26. Cooling field for FC protocol is 10 kOe. Complete ZFC hysteresis loops are depicted in the corresponding insets.

loops in the insets of Figs. 4(a)–4(i). For particles with dominant Co component at the particle core (samples 25 : 2, 24 : 3), the hysteresis loop exhibits the typical shape of a FM material, being reversible well below 20 kOe, and the high field magnetization reaches values close to saturation for bulk Co [$\sim$ 162 emu/g; see Fig. 5(d)] [19]. With the increase of the oxide component at the shell, the loop shapes become more elongated with higher closure fields [26,39] and a high field linear component with increasing contribution. This high field susceptibility can be ascribed to the contribution of uncompensated spins in the antiferromagnetic shell and core/shell interface [43–45] as it dies off at temperatures higher than T_N of Co_3O_4. For the most oxidized sample (sample 1 : 26) a linear field dependence extends over the whole field range as typically reported for purely antiferromagnetic nanoparticles or in bulk [34,43,46].

In order to probe the effect of the shell thickness on the EB effect, all nine samples were cooled in $H_{\rm cool} = 10$ kOe from 300 K down to 5 K and magnetic hysteresis loops were recorded subsequently. The main panels in Figs. 4(a)–4(i) show a zoom of the central portion of the hysteresis loops for ZFC (continuous lines) and FC (dashed lines) protocols. Note that hysteresis loops after FC appear clearly shifted to the negative fields with respect to ZFC ones as a consequence of the EB coupling between the FM core and AF shell spins. In some cases, a vertical displacement is also observed. The EB field and vertical shift are defined as $H_E = (H_C^+ + H_C^-)/2$, $M_E = [M(20\ \text{kOe}) + M(-20\ \text{kOe})]/2$, respectively, where H_C^+ and H_C^- are the coercive fields at the decreasing and increasing field loop branches. The dependence of these quantities as well as that of the coercive field H_C and saturation magnetization M_S on the crystallite size of both phases is presented in Figs. 5(a)–5(d).

A first notable feature is the nonmonotonic behavior of H_E and H_C presented in Figs. 5(a) and 5(b), which has been reported previously for Co/CoO nanoparticles [8,40,46,47]. An argument based on an energetic balance between exchange coupling and anisotropy in coupled FM/AF thin films with ideal interfaces indicate that EB should grow following a $1/d_{FM}$ law [6] when the thickness of the FM is reduced, resulting from the increase in surface to volume ratio of the FM. However, it should be noted that this simple behavior may not be followed in a NP with fixed shell thickness due to their finite size and to the peculiar geometry of the interface [7].

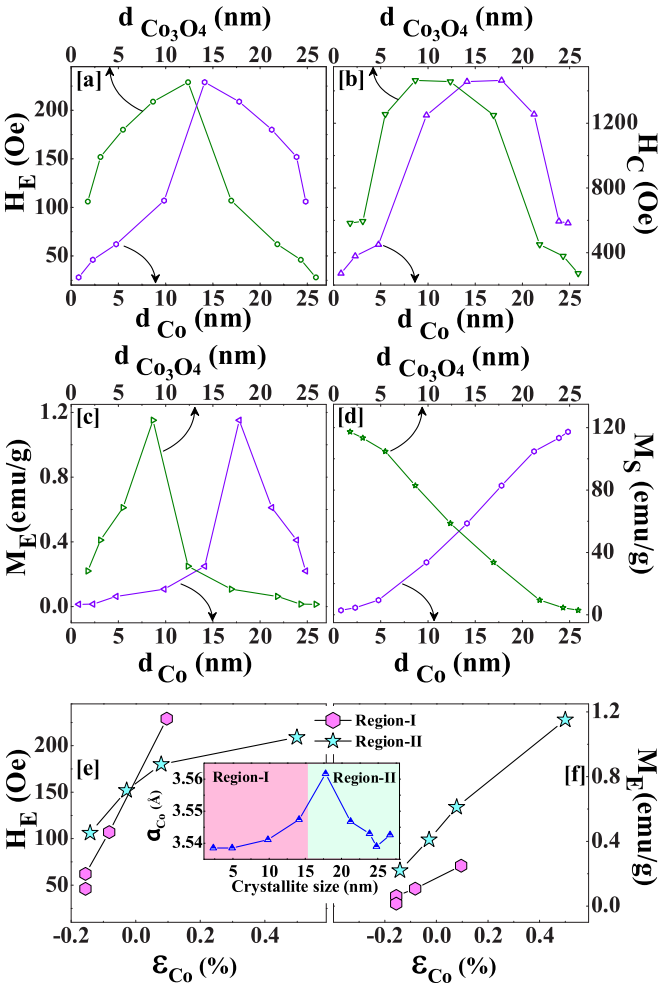

FIG. 5. Variation of (a) H_E, (b) H_C, (c) M_E, and (d) M_S with crystallite sizes of Co (d_{Co}) and Co_3O_4 ($d_{Co_3O_4}$). Panels (e) and (f) show the variation of H_E and M_E with Co lattice strain (ε_{Co}) at different regions of variation of the lattice parameter (a) indicated in the insets.

Moreover, it has been shown that in a NP with fixed core diameter, there should be a minimum critical shell thickness for the observation of a loop shift [8] and that, above it, H_E should increase with d_{Sh} up to a value above which it would become almost independent of d_{Sh}. In our case, however, we have NP with similar mean average sizes and varying shell thicknesses, so that we should expect an influence of this parameter on EB, based purely on finite-size effects, as we will clarify through the results of MC simulations that will be presented in Sec. V.

Apart from the above mentioned arguments, it should be noted that the maximum H_E and M_E is found for the sample with 18 : 9 composition, which was the one showing higher lattice mismatch. Therefore, lattice strain at the core/shell interface for the intermediate shell thickness might be also playing a role by inducing a higher net magnetic moment at the interface.

In order to better display this correlation, we have plotted the H_E and M_E dependences on strain (ε_{Co}), defined as $\varepsilon_{Co} = (a_{Co} - a_{Co-bulk})/a_{Co-bulk}$ in Figs. 5(e) and 5(f). Inset of those

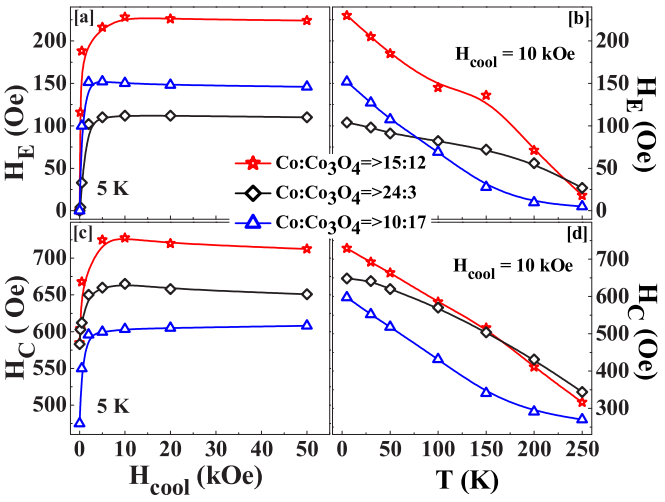

FIG. 6. Cooling field (H_{cool}) dependence of (a) H_E and (c) H_C and temperature variation of (b) H_E and (d) H_C for three selected samples as indicated in the legend.

figures describes region-I and region-II as those below and above the peak observed in the crystallite size dependence of a_{Co}. The dependence of H_E and M_E on ε_{Co} for region-I and region-II reveals that EB increases monotonously with the strain ascribed to the Co lattice mismatch.

These observations are in agreement with what has been found also at the interface of Au-Fe_3O_4 composites [48,49], Co/Co_3O_4 nanooctahedra [25], and Fe oxidized cubic NP [50], suggesting that lattice mismatch correlates with changes in magnetic anisotropy. There is also evidence that lattice strain induced by acoustic waves applied to some magnetic structures [51,52] can influence the value of the anisotropy constant and its easy axis. However, it is not clear how magnetoelastic coupling should be introduced to model structural changes at the core/shell interface of a NP, neither from experimental results nor from first principle calculations.

The coercive field H_C is also maximum for sample 18 : 9 as shown in Fig. 5(b), in correspondence with that observed for H_E and in agreement with the results of the MC simulations presented in Sec. V. Finally, we notice that vertical loop shifts indicated in Fig. 5(c) are concomitant to the observation of horizontal shifts and indicate the existence of a fraction of spins that remain pinned during the field reversal (see also the simulation results in Fig. 7 below). Therefore, the coincidence of the maximum for both quantities points to a relation between the increased interfacial anisotropy and stress as commented above.

We have also measured the thermal variation of FC hysteresis loops by cooling the samples while applying a 10 kOe magnetic field from 300 K down to different temperatures below 250 K and the H_{cool} dependence by cooling the samples from 300 K down to 5 K in different cooling fields up to 50 kOe. The extracted H_E and H_C values and their variation with the mentioned parameters are presented in Figs. 6(a) and 6(c) for 24 : 3, 15 : 1,2, and 10 : 17 samples. The values of H_E and H_C increase rapidly with H_{cool} initially and saturate for $H_{cool} > 10$ kOe for the three selected samples [see panels (a) and (c) in Fig. 6]. Therefore, we can exclude that the observed

loop shifts are due to minor loop effects. No maximum in these quantities has been detected, in contrast with what is observed in some studies of single phase oxide nanoparticles [53–55], where it was related to the glassy magnetic nature of surface spins.

The results displayed in Figs. 6(b) and 6(d) show that both H_E and H_C decrease with increasing temperature, although following different tendencies depending on the sample. Remarkably, although the Néel temperature of Co_3O_4 is below 40 K, the loop shifts persist up to ∼250 K or above, demonstrating the robustness of the exchange coupling between core and shell and the persistence of EB effects up to almost room temperature. Previous reports on the EB effect in systems with coexisting Co/Co_3O_4 phases indicated that a minor presence of CoO led to the persistence of EB much above its T_N [24–29]. Analogously, persistence of EB above T_N was also observed in Co/FeF_2 [56] and was explained by retention of short range magnetic ordering above T_N. Enhancement of the blocking temperature induced by EB was reported in $Fe_{0.6}Zn_{0.4}F_2$ (110)/Fe 14 nm/Ag 35 nm heterostructures [57], where it was attributed to the presence of Griffiths phase–like finite clusters. A coercivity enhancement was also reported in layered Fe/FeF_2 above T_N, which was suggested to be due to the growth of spin fluctuations in the antiferromagnetic FeF_2 [58].

V. SIMULATION RESULTS

To sustain the experimentally observed variation of H_E and H_C with particle morphology, we have conducted atomistic MC simulations of a model of core/shell nanoparticle [26,59] based on the following Hamiltonian:

$$\mathcal{H} = -\sum_{\langle i,j\rangle} J_{ij}\vec{S}_i\cdot\vec{S}_j - \sum_i K_i(\vec{S}_i\cdot\hat{n}_i)^2 - \sum_i \vec{S}_i\vec{h}, \qquad (1)$$

where $\vec{S}_i$ are Heisenberg classical unit vectors representing the magnetic ions and, in the last term, the magnitude of the magnetic field $\vec{H}$ is given in reduced units $h = \mu_S H$, with μ_S the atomic spin moment. Note also that all parameters used in the simulations will be given in temperature units, scaling them by the Boltzmann constant k_B and that the simulation temperature includes a factor $1/S^2$. The real values of the exchange and anisotropy constants for Co and Co_3O_4 have been used [60] and they are given by $J_C = 92.75$ K, $J_{Sh} = 0.23J_C$, and $K_{Sh} = 40.1J_C, K_C = 0.022J_C$. The interface exchange coupling has been set to $J_{\rm int} = -J_C$. The total radius of the simulated particles (containing 212095 spins) has been taken as the mean radius of the real samples $R = 38a$ (where a is the lattice constant) and nine shell thicknesses $t_{sh}/a = 2.4, 4.4, 7.7, 12.3, 17.5, 23.8, 30.8, 34.6, 36.5$ have been considered as studied experimentally. In order to mimick the observed presence of crystallites in the shell of the real nanoparticles (see Sec. III), we have divided the shell in regions with different random anisotropy directions similar to what was done in the literature [26,59]. This turns out to be crucial to reproduce the experimental phenomenology.

In Fig. 7(a), we present the simulated hysteresis loops as obtained after cooling down to 0.1 K under an applied magnetic field, $h_{FC} = 10$ K, for different shell thicknesses. The loops

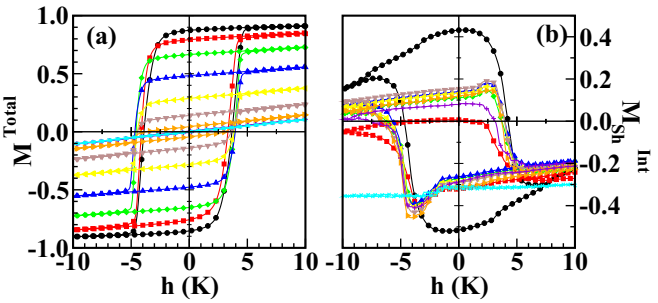

FIG. 7. Simulated hysteresis loops for individual particles with the same dimensions as experimental samples with increasing shell thickness from outer to innermost loops. Panel (a) shows the normalized magnetization of the whole particle. Panel (b) shows the contribution of the interfacial spins at the shell.

display shifts contrary to the cooling field direction, that vary in a nonmonotonous way with t_{sh}. With increasing t_{sh} the fraction of AF spins increases. As a result of it, the remanent magnetization decreases and the loops become more similar to that of an AF material. The area of the loops decrease with an extended region having linear field dependence, in qualitative agreement with the experimentally observed behavior.

The variation of the EB field can be more easily traced back to the magnetization reversal behavior of the interfacial spins at the shell [61], whose contribution to the hysteresis loop is shown in Fig. 7(b). As can be clearly seen, the interfacial shell hysteresis loops present a clear asymmetry between the decreasing and increasing field branches and, some of them, display characteristic apexes near the coercive field points [16,61]. Although the interface shell magnetization remains quite constant except near the coercive fields, on the decreasing field branch it is not equal (in absolute value) to that on the increasing field. This indicates that a considerable fraction of interfacial shell spins remains pinned during the field reversal. This can be directly checked by looking at snapshots of the spin configurations at the interface taken at different points of the hysteresis loops, as displayed in Fig. 8 for a particle with $t_{sh}/a = 17.5$. Comparing the magnetic configurations at the remanent [panels (a) and (c)] and coercive field points [panels (b) and (d)], we can see that the interfacial surface spins remain mostly oriented along the direction induced by the magnetic field applied during the initial cooling, as indicated by the absence of variation in the colors of the outer shell of spins. On the contrary, interfacial core spins (the ones in the inner part of the interface in Fig. 8) are dragged during the quasiuniform core reversal as can be appreciated by the change in color (reddish to bluish and vice versa) and orientation when going from remanent to the coercive field points.

In order to compare with the experimental results of Figs. 5 and 6, we have calculated the coercive field and horizontal loop shifts as $h_C = (h_c^+ - h_c^-)/2$, $h_E = (h_c^+ + h_c^-)/2$ from the hysteresis loops of Fig. 7. Their dependence on the core diameter is given in Fig. 9. Initially, both the quantities increase with increasing the particle core diameter starting from a fully AF particle corresponding to the increase of the interfacial region surface, as it is also observed experimentally. However,

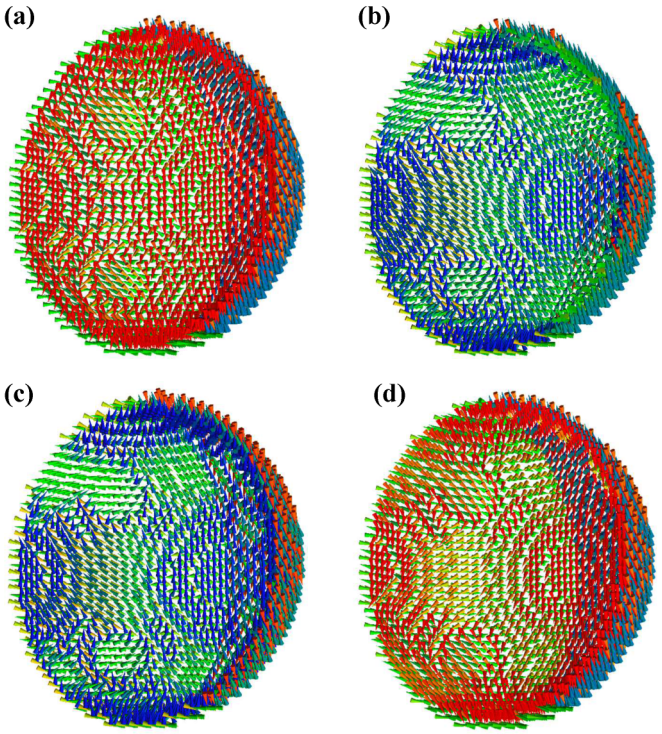

FIG. 8. Snapshots of a slice of a nanoparticle with $t_{sh}/a = 17.5$ (sample with 15 : 12 composition) showing the interfacial spin magnetic configurations at different points of the hysteresis loop (from left to right): (a) positive remanence point, (b) negative coercive field, (c) negative remanent point, and (d) positive coercive field. Cone colors vary depending on their component along the field direction from red (along the field direction) to blue (contrary to the field direction) following the visible light spectrum.

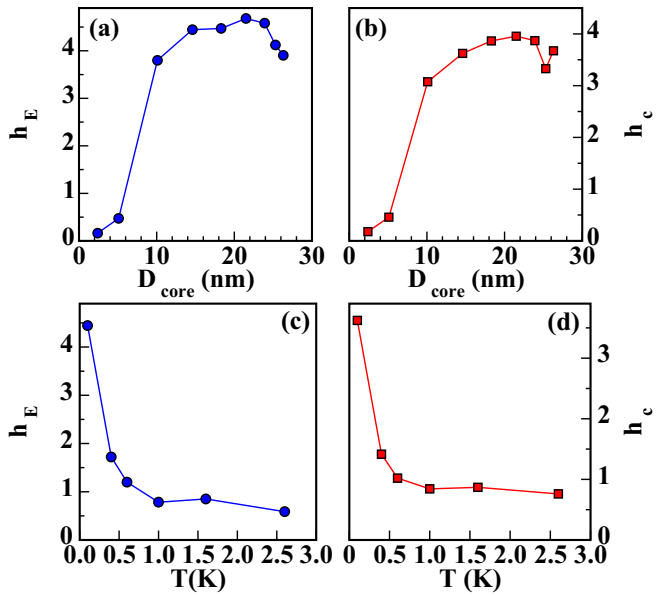

FIG. 9. Upper panels show the variation of (a) the shift h_E and (b) coercive field h_C of the simulated hysteresis loops with the diameter of the particle core. Lower panels show the thermal dependence of (c) h_E and (d) h_C for a particle with shell size $t_{\text{shell}} = 17a$.

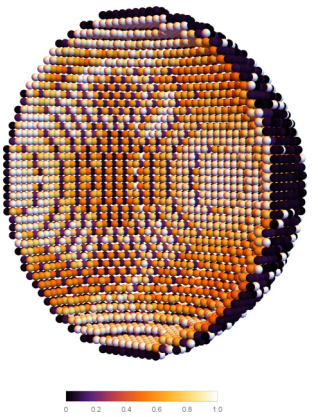

FIG. 10. Snapshot showing a cut of the interfacial spin positions represented by spheres. Sphere coloring varies with the normalized magnitude of the difference between local spin orientations at the two coercive field points. Lighter color means more difference.

this tendency is broken as the core size increases further and a maximum in h_E is observed for a core diameter of 20 nm (shell thickness of 6 nm). Below this value, the EB field progressively decreases as the shell thickness is reduced. This nonmonotonous trend is in agreement with that observed experimentally although simulations cannot explicitly take into account the effects of stress on the spin lattice. As mentioned at the end of Sec. IV, in order to do so, we would need additional input coming from *ab initio* calculations that, in principle, would be able to correlate structural relaxation (stress) to changes in J and K. However, presently available first principle methods are not able to do this even for clusters with more than some tenths of atoms.

The observed behavior for h_E correlates with the changes in the contribution of the interfacial surface spins to the hysteresis loops displayed in Fig. 7(b), where it can be seen that the change in the fraction of pinned spins decreases for the particles with thinner shells (black, red, and green curves) as compared to the one giving maximum EB (blue curve). A similar trend is observed for the h_C curve, which can be understood by noticing that the coercive field, at difference from h_E, is directly related to the reversal of the core spins, as can be observed in Fig. 10, where a snapshot of the local changes in spin orientations between the positive and negative coercive field is depicted. The reversal of the core drags some of the core (inner) spins at the interface, which explains the increase of h_C with D_{core}. In contrast, spins at the outer part of the interface remain pinned, thus contributing to the loop shift. Finally, let us also remark that the results of the hysteresis loops at finite temperatures for sample with $t_{\text{shell}} = 17.5a$ shown in Figs. 9(c) and 9(d) indicate a thermal dependence h_E and h_C which is in agreement with the monotonous decrease also observed experimentally.

VI. CONCLUSIONS

We have reported synthesis of Co based NP in a silica matrix with core/shell structure through a controlled oxidation method, giving evidence that the shell is formed by crystallites having only the Co_3O_4 phase contrary to most reported studies

where the main phase is CoO. Absence of this phase in our NP has been confirmed by XRD, TEM, and XPS spectroscopic techniques. We have prepared batches of NP with different shell thickness but controlling the mean total NP diameter and keeping the dispersion in the matrix at 10% volume fraction to minimize the influence of interparticle interactions and studied the changes in the magnetic properties as t_{Sh} is varied. The maximum in the EB and coercive fields has been observed for the samples with intermediate shell thickness, which has been correlated to the observation of a maximum value of the strain at the core/shell interface. Although the Co_3O_4 phase has much lower ordering temperature than CoO, we have reported the existence of EB bias effects that persist up to almost room temperature. The experimental results have been complimented with MC simulations based on atomistic spin model of an individual NP with varying AF shell thickness of sizes comparable to those studied experimentally. The simulation results reproduced qualitatively the observed EB phenomenology regarding the variation of H_E and H_C with t_{Sh} and their temperature dependence, and suggest that the microsocopic changes in the interface pinning mechanism as t_{Sh} is varied, that induce changes in the magnetization reversal of the interfacial shell spins, determine the EB effect and its dependence on the specific material parameters as well as geometry of the NP.

ACKNOWLEDGMENTS

S. G. wishes to thank DST, India (Project No. SB/S2/CMP-029/2014) for the financial support. SQUID magnetometer of Quantum Design and TEM are used in this study under DST the project, Unit of Nanoscience at Indian Association for the Cultivation of Science, Jadavpur, India. O.I. acknowledges financial support form the Spanish MINECO [Grants No. MAT2012-33037 and No. MAT2015-68772-P (MINECO/FEDER)], Catalan DURSI (Grant No. 2014SGR220), and European Union FEDER Funds (Una manera de hacer Europa); also CSUC for supercomputer facilities.

[1] J. L. Dormann, D. Fiorani, and E. Tronc, Magnetic relaxation in fine-particle systems, Adv. Chem. Phys. **98**, 283 (1997).

[2] R. H. Kodama, Magnetic nanoparticles, J. Magn. Magn. Mater. **200**, 359 (1999).

[3] D. Fiorani, *Surface Effects in Magnetic Nanoparticles* (Springer US, Boston, MA, 2005).

[4] Ò. Iglesias and A. Labarta, Finite-size and surface effects in maghemite nanoparticles: Monte Carlo simulations, Phys. Rev. B **63**, 184416 (2001).

[5] Z. Sabsabi, F. Vernay, O. Iglesias, and H. Kachkachi, Interplay between surface anisotropy and dipolar interactions in an assembly of nanomagnets, Phys. Rev. B **88**, 104424 (2013).

[6] J. Nogués and I. K. Schuller, Exchange bias, J. Magn. Magn. Mater. **192**, 203 (1999).

[7] J. Nogués, J. Sort, V. Langlais, V. Skumryev, S. Suriñach, J. S. Muñoz, and M. D. Baró, Exchange bias in nanostructures, Phys. Rep. **422**, 65 (2005).

[8] Ò. Iglesias, A. Labarta, and X. Batlle, Exchange bias phenomenology and models of core/shell nanoparticles, J. Nanosci. Nanotechnol. **8**, 2761 (2008).

[9] S. Giri, M. Patra, and S. Majumdar, Exchange bias effect in alloys and compounds, J. Phys.: Condens. Matter **23**, 073201 (2011).

[10] P. K. Manna and S. M. Yusuf, Two interface effects: Exchange bias and magnetic proximity, Phys. Rep. **535**, 61 (2014).

[11] M. Gierlings, M. J. Prandolini, H. Fritzsche, M. Gruyters, and D. Riegel, Change and asymmetry of magnetization reversal for a Co/CoO exchange-bias system, Phys. Rev. B **65**, 092407 (2002).

[12] V. Skumryev, S. Stoyanov, Y. Zhang, G. Hadjipanayis, D. Givord, and J. Nogués, Beating the superparamagnetic limit with exchange bias, Nature (London) **423**, 850 (2003).

[13] S. G. E. te Velthuis, A. Berger, G. P. Felcher, B. K. Hill, and E. Dan Dahlberg, Training effects and the microscopic magnetic structure of exchange biased Co/CoO bilayers, J. Appl. Phys. **87**, 5046 (2000).

[14] F. Radu, M. Etzkorn, R. Siebrecht, T. Schmitte, K. Westerholt, and H. Zabel, Interfacial domain formation during magnetization reversal in exchange-biased CoO/Co bilayers, Phys. Rev. B **67**, 134409 (2003).

[15] S. Das, M. Patra, S. Majumdar, and S. Giri, Exchange bias effect at the irregular interfaces between Co and CoO nanostructures, J. Alloys Compd. **488**, 27 (2009).

[16] M. H. Wu, Q. C. Li, and J.-M. Liu, Monte Carlo simulation of size, random field and temperature dependences of exchange bias in a core/shell magnetic nanoparticle, J. Phys.: Condens. Matter **19**, 186202 (2007).

[17] C. Chappert, A. Fert, and F. N. Van Dau, The emergence of spin electronics in data storage, Nat. Mater. **6**, 813 (2007).

[18] A. López-Ortega, M. Estrader, G. Salazar-Alvarez, A. G. Roca, and J. Nogués, Applications of exchange coupled bimagnetic hard/soft and soft/hard magnetic core/shell nanoparticles, Phys. Rep. **553**, 1 (2015).

[19] R. C. O'Handley, *Modern Magnetic Materials: Principles and Applications* (John Wiley and Sons, New York, 2000).

[20] K. Haneda and A. H. Morrish, Oxidation of aerosoled ultrafine iron particles, Nature (London) **282**, 186 (1979).

[21] S. Giri, S. Ganguli, and M. Bhattacharya, Surface oxidation of iron nanoparticles, Appl. Surf. Sci. **182**, 345 (2001).

[22] J. B. Goodenough, *Magnetism and the Chemical Bond* (Interscience Publishers, New York, 1963).

[23] W. H. Meiklejohn and C. P. Bean, New magnetic anisotropy, Phys. Rev. **102**, 1413 (1956).

[24] N. Fontaiña Troitiño, S. Liébana-Viñas, B. Rodríguez-González, A. Kovács, Z.-A. Li, M. Spasova, M. Farle, and V. Salgueiriño, Room-temperature ferromagnetism in antiferromagnetic cobalt oxide nanooctahedra, Nano Lett. **14**, 640 (2014).

[25] Z.-A. Li, N. Fontaiña Troitiño, A. Kovács, S. Liébana-Viñas, M. Spasova, R. E. Dunin-Borkowski, M. Müller, D. Doennig, R. Pentcheva, M. Farle, and V. Salgueiriño, Electrostatic doping

as a source for robust ferromagnetism at the interface between antiferromagnetic cobalt oxides, Sci. Rep. **5**, 7997 (2015).

[26] K. Simeonidis, C. Martinez-Boubeta, O. Iglesias, A. Cabot, M. Angelakeris, S. Mourdikoudis, I. Tsiaoussis, A. Delimitis, C. Dendrinou-Samara, and O. Kalogirou, Morphology influence on nanoscale magnetism of co nanoparticles: Experimental and theoretical aspects of exchange bias, Phys. Rev. B **84**, 144430 (2011).

[27] Y.-X. Wang, B. You, W. Tian, Y.-X. Wang, L. Sun, M. Lu, and Q. Li, Exchange bias and angular dependence in Co/Co_3O_4 bilayers, Int. J. Mod. Phys. B **19**, 2580 (2005).

[28] Y. Wang, W. Tian, Y. Wang, L. Sun, Q. Li, B. You, A. Hu, H. Zhai, and M. Lu, The effect of capping layer Ta on magnetic behavior for multilayers $Ta/Co/Co_3O_4/Ta$, Solid State Commun. **135**, 725 (2005).

[29] B. You, Y. Wang, Y. Zhao, L. Sun, W. Sheng, M. Pan, J. Du, A. Hu, and M. Lu, Exchange bias in Co/Co_3O_4 bilayers, J. Appl. Phys. **93**, 6587 (2003).

[30] Y. Wang, Y. Zhang, Y. Cao, M. Lu, and J. Yang, Properties of exchange biased Co/Co_3O_4 bilayer films, J. Alloys Compd. **450**, 128 (2008).

[31] H. Ahmadvand, S. R. Safdari, A. N. Golikand, P. Dasgupta, A. Poddar, and H. Salamati, Exchange bias in $Co/CoO/Co_3O_4$ nanostructures, J. Magn. Magn. Mater. **377**, 19 (2015).

[32] V. Bisht and K. P. Rajeev, Non-equilibrium effects in the magnetic behavior of Co_3O_4 nanoparticles, Solid State Commun. **151**, 1275 (2011).

[33] Y. Ichiyanagi and S. Yamada, The size-dependent magnetic properties of Co_3O_4 nanoparticles, Polyhedron **24**, 2813 (2005).

[34] P. Dutta, M. S. Seehra, S. Thota, and J. Kumar, A comparative study of the magnetic properties of bulk and nanocrystalline Co_3O_4, J. Phys.: Condens. Matter **20**, 015218 (2008).

[35] N. J. O. Silva, A. Millán, F. Palacio, M. Martins, T. Trindade, I. Puente-Orench, and J. Campo, Remanent magnetization in CoO antiferromagnetic nanoparticles, Phys. Rev. B **82**, 094433 (2010).

[36] B. D. Cullity and S. R. Stock, *Elements of X-ray Diffraction* (Pearson, Harlow, 2014).

[37] L. Zhuo, J. Ge, L. Cao, and B. Tang, Solvothermal synthesis of CoO, Co_3O_4, $Ni(OH)_2$ and $Mg(OH)_2$ nanotubes, Cryst. Growth Design **9**, 1 (2009).

[38] T. Nishizawa and K. Ishida, The Co (Cobalt) system, Bull. Alloy Phase Diagr. **4**, 387 (1983).

[39] S. Chandra, H. Khurshid, M.-H. Phan, and H. Srikanth, Asymmetric hysteresis loops and its dependence on magnetic anisotropy in exchange biased Co/CoO core-shell nanoparticles, Appl. Phys. Lett. **101**, 232405 (2012).

[40] M. Feygenson, Y. Yiu, A. Kou, K.-S. Kim, and M. C. Aronson, Controlling the exchange bias field in Co core/CoO shell nanoparticles, Phys. Rev. B **81**, 195445 (2010).

[41] W. L. Roth, The magnetic structure of Co_3O_4, J. Phys. Chem. Solids **25**, 1 (1964).

[42] D. von Dreifus, E. C. Pereira, and A. J. A. de Oliveira, Observation of superficial antiferromagnetism in Co_3O_4 polycrystals, Mater. Res. Express **2**, 116102 (2015).

[43] J. B. Tracy, D. N. Weiss, D. P. Dinega, and M. G. Bawendi, Exchange biasing and magnetic properties of partially and fully oxidized colloidal cobalt nanoparticles, Phys. Rev. B **72**, 064404 (2005).

[44] J. B. Tracy and M. G. Bawendi, Defects in CoO in oxidized cobalt nanoparticles dominate exchange biasing and exhibit anomalous magnetic properties, Phys. Rev. B **74**, 184434 (2006).

[45] N. Rinaldi-Montes, P. Gorria, D. Martínez-Blanco, Z. Amghouz, A. B. Fuertes, L. Fernández Barquín, J. Rodríguez Fernández, L. Olivi, G. Aquilanti, and J. A. Blanco, Disentangling magnetic core/shell morphologies in Co-based nanoparticles, J. Mater. Chem. C **4**, 2302 (2016).

[46] M. Kovylina, M. G. del Muro, Z. Konstantinovic, M. Varela, Ò. Iglesias, A. Labarta, and X. Batlle, Controlling exchange bias in $Co\text{-}CoO_x$ nanoparticles by oxygen content, Nanotechnology **20**, 175702 (2009).

[47] S. Gangopadhyay, G. C. Hadjipanayis, C. M. Sorensen, and K. J. Klabunde, Exchange anisotropy in oxide passivated Co fine particles, J. Appl. Phys. **73**, 6964 (1993).

[48] S. Chandra, N. A. F. Huls, M. H. Phan, S. Srinath, M. A. Garcia, Y. Lee, C. Wang, S. Sun, Ò. Iglesias, and H. Srikanth, Exchange bias effect in $Au\text{-}Fe_3O_4$ nanocomposites, Nanotechnology **25**, 055702 (2014).

[49] M. Feygenson, J. C. Bauer, Z. Gai, C. Marques, M. C. Aronson, X. Teng, D. Su, V. Stanic, V. S. Urban, K. A. Beyer, and S. Dai, Exchange bias effect in $Au\text{-}Fe_3O_4$ dumbbell nanoparticles induced by the charge transfer from gold, Phys. Rev. B **92**, 054416 (2015).

[50] A. Pratt, L. Lari, O. Hovorka, A. Shah, C. Woffinden, S. P. Tear, C. Binns, and R. Kröger, Enhanced oxidation of nanoparticles through strain-mediated ionic transport, Nat. Mater. **13**, 26 (2013).

[51] O. Kovalenko, T. Pezeril, and V. V. Temnov, New Concept for Magnetization Switching by Ultrafast Acoustic Pulses, Phys. Rev. Lett. **110**, 266602 (2013).

[52] V. Sampath, N. D'Souza, D. Bhattacharya, G. M. Atkinson, S. Bandyopadhyay, and J. Atulasimha, Acoustic-wave-induced magnetization switching of magnetostrictive nanomagnets from single-domain to nonvolatile vortex states, Nano Lett. **16**, 5681 (2016).

[53] L. Del Bianco, D. Fiorani, A. Testa, E. Bonetti, and L. Signorini, Field-cooling dependence of exchange bias in a granular system of Fe nanoparticles embedded in an Fe oxide matrix, Phys. Rev. B **70**, 052401 (2004).

[54] D. Fiorani, L. Del Bianco, A. M. Testa, and K. N. Trohidou, Exchange bias in disordered granular systems, J. Phys.: Condens. Matter **19**, 225007 (2007).

[55] M. Vasilakaki and K. N. Trohidou, Numerical study of the exchange-bias effect in nanoparticles with ferromagnetic core/ferrimagnetic disordered shell morphology, Phys. Rev. B **79**, 144402 (2009).

[56] M. Grimsditch, A. Hoffmann, P. Vavassori, H. Shi, and D. Lederman, Exchange-Induced Anisotropies at Ferromagnetic-Antiferromagnetic Interfaces Above and Below the Néel Temperature, Phys. Rev. Lett. **90**, 257201 (2003).

[57] X. Chen, C. Binek, A. Hoshstrat, and W. Kleemann, Dilution-induced enhancement of the blocking temperature in exchange-bias heterosystems, Phys. Rev. B **65**, 012415 (2001).

[58] C. Leighton, H. Suhl, M. J. Pechan, R. Compton, J. Nogués, and I. K. Schuller, Coercivity enhancement above the Néel temperature of an antiferromagnet/ferromagnet bilayer, J. Appl. Phys. **92**, 1483 (2002).

[59] A. Cabot, A. P. Alivisatos, V. F. Puntes, L. Balcells, Ò. Iglesias, and A. Labarta, Magnetic domains and surface effects

in hollow maghemite nanoparticles, Phys. Rev. B **79**, 094419 (2009).

[60] L. Balcells, B. Martínez, Ò. Iglesias, J. M. García-Martín, A. Cebollada, A. García-Martín, G. Armelles, B. Sepúlveda, and Y. Alaverdyan, Magnetic domains and surface effects in hollow maghemite nanoparticles, Appl. Phys. Lett. **94**, 062502 (2009).

[61] Ò. Iglesias, X. Batlle, and A. Labarta, Microscopic origin of exchange bias in core/shell nanoparticles, Phys. Rev. B **72**, 212401 (2005).